

Hierarchically Assembled Tubular Shell-Core-Shell Heterostructure of Hybrid Transition Metal Chalcogenides for High-Performance Supercapacitors with Ultrahigh Cyclability

Young-Woo Lee^{a,1}, Byung-Sung Kim^{a,1}, John Hong^a, Heechae Choi^b, Hyun-Sik Jang^c, Bo Hou^a, Sangyeon Pak^a, Juwon Lee^a, Sang-Hyo Lee^a, Stephen M. Morris^a, Dongmok Whang^c, Jin-Pyo Hong^d, Hyeon Suk Shin^e, SeungNam Cha^{a,*}, Jung Inn Sohn^{a,*}, Jong Min Kim^f

^a Department of Engineering Science, University of Oxford, Oxford OX1 3PJ, United Kingdom.

^b Center for Computational Science, Korea Institute of Science and Technology, Seoul 02792, Republic of Korea.

^c School of Advanced Materials Science and Engineering, SKKU Advanced Institute of Nanotechnology (SAINT), Sungkyunkwan University, Gyeonggi-Do 16419, Republic of Korea.

^d Research Institute of Convergence of Basic Science, Novel Functional Materials and Device Laboratory, Department of Physics, Hanyang University, Seoul 15588, Republic of Korea.

^e Department of Chemistry, Ulsan National Institute of Science and Technology (UNIST), Ulsan 44919, Republic of Korea.

^f Electrical Engineering Division, Department of Engineering, University of Cambridge, Cambridge CB3 0FA, United Kingdom.

¹ These authors contributed equally to the work.

*Corresponding Author

E-mail: seungnam.cha@eng.ox.ac.uk (S.N.C.) and junginn.sohn@eng.ox.ac.uk (J.I.S.).

ABSTRACT.

Pseudo-capacitive transition metal chalcogenides have recently received considerable attention as a promising class of materials for high performance supercapacitors (SCs) due to their superior intrinsic conductivity to circumvent the limitations of corresponding transition metal oxides with relatively poor conductivity. However, the important challenge associated with the utilization of such high-capacitive electrode materials is the development of desirably structured electrode materials, enabling efficient and rapid Faradaic redox reactions and ultra long-term cycling. Here, we propose a hierarchically integrated hybrid transition metal (Cu-Ni) chalcogenide shell-core-shell (HTMC-SCS) tubular heterostructure using a facile bottom-up synthetic approach. The resultant HTMC-SCS electrode exhibits a high volumetric capacitance of 25.9 F cm^{-3} at a current density of 2 mA cm^{-2} . Furthermore, asymmetric SCs based on an HTMC-SCS heterostructured electrode demonstrate a high power density (770 mW cm^{-3}) and an energy density (2.63 mWh cm^{-3}) as well as an ultrahigh reversible capacity with a capacitance retention of 84% and a long-term cycling stability of over 10000 cycles. Based on experimental results and density functional theory calculations, these remarkably improved electrochemical features are discussed and explained in terms of the unique combination of the conductive CuS core and active NiS shell materials, hierarchical tubular open geometry with nanoscale inner/outer shell structure, and mechanical stress-mitigating interlayer on shell-core-shell interface, allowing highly reversible and efficient electrochemical redox processes coupled with fast charge transfer kinetics and an electrochemically stable structure.

KEYWORDS. heteroatom transition metal chalcogenide; tubular shell-core-shell; hierarchical heterostructure; electrochemical performance; supercapacitor.

1. Introduction.

The rapid technological advances in areas such as electrical vehicles, high energy consuming portable electronics, and energy back-up systems for emergency and unbalanced power supplies for both day and night, have triggered tremendous efforts to develop an innovative energy storage system for meeting the ever-increasing global demands for high energy and power density needs [1,2]. In this regard, supercapacitors (SCs) that can electrochemically store charge and deliver energy with a high power density and ultrahigh reversible cyclability have become crucially important as one of the most promising energy storage systems to complement or replace batteries [3]. Particularly, pseudo-capacitive SCs, which are operated through a reversible Faradaic redox mechanism, essentially require electrode materials with various valance states, good electrical conductivity, and large surface areas. Therefore, previous work has focused on identifying suitable pseudo-capacitive materials with a desirable Faradaic redox balance, such as transition metal based oxide/hydroxide, by considering the design of novel electrodes with hierarchical structures to simultaneously maximize the active surface area, the charge transport kinetics, and the cycle stability [4]. As a result, it is anticipated that superior pseudo-capacitive performance such as a high specific capacitance and a high rate performance as well as an ultrahigh cyclability during the charge/discharge process could be realized.

Recently, transition metal chalcogenides, such as CoS [5], SnS [6], ZnS [7], and MnS [8], have been considered and investigated for next-generation pseudo-capacitive SCs. Among them, nickel chalcogenide (NiS) has been shown to be a promising candidate for pseudo-capacitive electrodes since it has a superior intrinsic electrical conductivity and a high specific capacitance based on the active Faradaic redox reaction of $\text{Ni}^{2+}/\text{Ni}^{3+}$, resulting in an enhanced energy density [9-12]. However, it has been reported that the NiS electrode exhibits serious capacitance fading because

of its low structural stability induced by the electrosorption and intercalation reaction process, which produces an acute internal mechanical stress during the charge-discharge cycling. To date, several investigations have been carried out to address the issues related to the structural instability of NiS each involving a different approach, such as electrode-structure engineering and hybrid electrodes combined with other transition metal oxide/chalcogenide materials or nanostructured carbon materials [11-13]. However, it is still challenging yet highly desirable to develop an effective and practical strategy to achieve excellent electrochemical performances without sacrificing the stability of the electrode structure.

Herein, we report a new approach for designing and developing a novel hierarchical heterostructure of hybrid transition metal (Cu and Ni) chalcogenide shell-core-shell (HTMC-SCS) electrode materials, consisting of an electrochemically stable CuS hollow nanotube as a core structure and a superior pseudo-capacitive NiS nanoscale-thin layer as an inner/outer shell structure, directly grown on a Cu mesh current collector via a free-standing growth method. In particular, we have carefully selected two different metal chalcogenide materials and designed the hierarchical core-shell SC electrodes by considering the parameters that are important for evaluating the feasibility of such an electrode as indicated in the radar plot of Fig. 1a [14-18].

In spite of the relatively low capacitance of the CuS electrode materials, their superior electrical conductivity, good rate property, and high structural stability as well as their low cost make them promising materials for the use as the core material, leading to a superior long-term stability under electrochemical cycling conditions [19]. NiS electrode materials, on the other hand, exhibit excellent capacitive properties due to their electrochemically superior reactivity with the OH^- ions. Thus, the novel hierarchical HTMC-SCS electrode architecture is systematically designed to simultaneously demonstrate excellent cyclability and energy storage capability, as illustrated in

Fig. 1b. Firstly, the nanoscale NiS shell layer on the inner/outer surface of the hollow tubular core structure allows for an enlarged electrochemically active surface area and a shortened ion diffusion distance, resulting in an improved energy density. Secondly, the directly grown HTMC-SCS electrodes with highly conductive CuS core materials on the current collector not only provide a favorable conductive pathway for efficient charge transport but also facilitate fast ion diffusion and facile electrolyte permeation, consequently resulting in a high rate performance and an enhanced power density. Thirdly, the unique hierarchical tubular structures with a well-defined pore space and an energetically stable core-shell intermediate region can tolerate any possible structural variation as well as accommodate any mechanical stress during the charge/discharge process, thereby ensuring the excellent cyclability. We have also demonstrated that the electrochemically pseudo-capacitive characteristics of the HTMC-SCS electrode are strongly dependent on the NiS shell layer structure through an investigation of the kinetic relationship between the OH^- ion diffusion behavior and the shell thickness. Finally, we have demonstrated that the asymmetric supercapacitor (ASC) based on the HTMC-SCS heterostructure exhibits superior electrochemical properties including a high maximum energy (2.63 mWh cm^{-3}) with power (770 mW cm^{-3}) densities and the ultrahigh cyclability up to the 10000 cycles that are comparable to commercial energy storage devices.

2. Results and Discussion

In order to achieve a well-organized NiS/CuS/NiS shell-core-shell heterostructure directly grown on a current collector, we employed a hierarchical two-step synthesis approach followed by the sulfurization process at each synthetic step. $\text{Cu}(\text{OH})_2$ nanotubes were first prepared by using a free-stranding growth method so as to employ as a template for the production of the core CuS

nanotube arrays **with well-defined tubular structure and stoichiometry**. As shown in the scanning electron microscopy (SEM) images of Fig. 1c, the well-defined hollow structure of the 1-dimensional Cu(OH)₂ nanotubes was observed. Fig. 1f shows that all the X-ray diffraction (XRD) peaks of the Cu(OH)₂ nanotubes correspond to the orthorhombic Cu(OH)₂ phase (JCPDS No. 13-0420) and confirm the formation of a highly crystalline structure. Then, the CuS nanotubes were obtained without a specific aggregation amongst the nanostructures and the structural collapse through the sulfurization process based on anion exchange reactions as indicated in Fig. 1d. Moreover, the XRD patterns of a CuS nanotube sample are well indexed to the hexagonal CuS phase (JCPDS No. 06-0464, Fig. 1g and S1a). It is highly expected that such a crystalline CuS will contribute to the cyclability improvements of the SCs due to its excellent structural feature and electrochemical stability. Lastly, to maximize the active sites for pseudo-capacitive reactions, nanoscale NiS shell layers coated on both the whole of the inner and outer CuS nanotube walls were fabricated through sequential Ni and S species adsorption processes by the dip-coating of the as-produced CuS nanotube **so as to obtain the HTMC-SCS electrode materials with hierarchically well-defined, uniform tubular heterostructures** as shown in Fig. 1e. It is also clearly confirmed that the synthesized NiS shell exhibits a hexagonal-structured α -NiS phase, as shown by the XRD patterns (JCPDS No. 02-1280) in Fig. 1h and S1b.

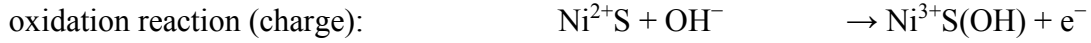
The detailed morphology and structural features of the HTMC-SCS were further investigated using transmission electron microscopy (TEM) as shown in Fig. 2a. It can be seen that the HTMC-SCS has a well-defined hollow tubular nanostructure with a pore diameter of ~30 nm and an overall wall thickness of ~50 nm, whereby the tubular wall consists of the inner/outer NiS shells (the light gray region) and the CuS core (the relatively dark region). Furthermore, the energy dispersive X-ray spectroscopy (EDX) line-scanning profiles (Fig. 2b) and the EDX mapping profile (Fig. 2c)

evidently confirm that nanoscale thin NiS shell layers (approximately 10-15 nm) are formed on the inner and outer wall of the CuS nanotube. Note that unlike previously reported core-shell nanowires with only a single outer shell layer [20-22], our unique hierarchical HTMC-SCS architecture with a tubular structure can increase the utilization of the active electrode materials through the inner/outer NiS shell layer structure and can provide an efficient OH⁻ ion diffusion channel, thereby improving the pseudo-capacitive behavior for high volumetric energy and power densities.

The surface chemical state of the HTMC-SCS was determined by X-ray photoelectron spectroscopy (XPS), which reveals that the Cu 2p_{3/2} XPS spectrum exhibits two peaks centered at binding energies of 932.63 eV and 934.02 eV, corresponding to the Cu⁰ and Cu²⁺ states, respectively (Fig. 2d) [23,24]. The Ni 2p_{3/2} XPS spectrum was also clearly observed, which can be deconvoluted into two oxidized Ni states with a strong peak at 853.29 eV and a weaker peak at 854.90 eV, revealing the presence of Ni-S bond and oxidized Ni states, respectively (Fig. 2e) [23,25]. Moreover, it can be seen that the peak of S 2p_{3/2} with the binding energy at 162.0 eV corresponds to the combined metal-S bonds (Fig. 2f) [23]. These XPS results indicate that the Cu²⁺ ions are incorporated into both the tetrahedral and trigonal planar sites surrounded by S atoms in the hexagonal CuS crystal structure with a large internal space, whereas the Ni²⁺ ions are occupied by octahedral sites in the hexagonal NiS crystal system that will play an important role in the enhanced capability (see more detailed information in Fig. S1), which are consistent with XRD results in Fig. 1h.

The electrochemical pseudo-capacitive behaviors of the HTMC-SCS electrode were examined using cyclic voltammogram (CV) and galvanostatic charge/discharge measurements in a 1.0 M KOH electrolyte. Fig. 3a shows CV curves of the HTMC-SCS electrode in a wide operating

potential range from 0.0 to 0.7 V at a scan rate of 10 mV s⁻¹, exhibiting the typical Faradaic reaction features with a pair of strong symmetric redox peaks. It is suggested that the observed reversible redox pair is mainly related to the Faradaic redox reactions of NiS as follows [26,27]:



Note that although the CuS core material in HTMC-SCS electrodes can naturally act as the active site for the pseudo-capacitive behavior [19], the Faradaic redox peak related to intercalation reaction of OH⁻ ions into CuS was not observed in this study due to its relatively low specific capacitance compared to NiS as indicated in the inset of Fig. 3a. To further investigate the reversible pseudo-capacitive behavior of the HTMC-SCS electrode, we carried out CV measurements with increasing scan rates from 5 to 50 mV s⁻¹ as shown in Fig. 3b. It can be clearly seen that all the CV curves almost retain their original curve shape with the redox pair of Ni²⁺/Ni³⁺, indicating an ideal Faradaic behavior and a high Faradaic redox reaction reversibility.

To demonstrate the substantive electrochemical performance of the HTMC-SCS electrode, a galvanostatic charge/discharge evaluation was carried out within a range of 0.0 and 0.5 V at different current densities ranging from 2 to 20 mA cm⁻², as shown in Fig. 3c. The HTMC-SCS electrode exhibits a typical charge/discharge curve related to the reversible Faradaic redox reactions between Ni²⁺/Ni³⁺. Moreover, the volumetric capacitance of the HTMC-SCS electrode is found to be 25.9 F cm⁻³ at 2 mA cm⁻², which is considerably higher than that of previously reported pseudo-capacitive electrodes [28-30]. These results might be attributed to the unique nanoarchitecture structure with enlarged electrochemically active thin NiS shell layers existing on both the inner and outer surfaces of the electrically conductive tubular CuS core, allowing favorable OH⁻ ion diffusion and low contact resistance as well as large electrolyte contact areas.

Factually, we also confirmed that the HTMC-SCS electrode exhibits a very low charge transfer resistance of $0.23\ \Omega$ from the Nyquist plot obtained by electrochemical impedance spectroscopy (EIS, Fig. 3d and S2a). Moreover, we further showed that the diffusion coefficient (D) of the OH^- ions in the HTMC-SCS electrode is estimated to be $5.86 \times 10^{-9}\ \text{cm}^2\ \text{s}^{-1}$ from the Warburg impedance (see more detailed information in Fig. S2b) [31-33], which is excellent when compared to the D of other reported pseudo-capacitive electrodes with a range of $10^{-10} \sim 10^{-12}\ \text{cm}^2\ \text{s}^{-1}$ and lithium ion battery electrodes with a range of $10^{-11} \sim 10^{-16}\ \text{cm}^2\ \text{s}^{-1}$, as summarized in Table S1. Thus, we believe that our unique hierarchical structure with the desirable core-shell electrode materials and geometry is beneficial to the charge transfer kinetics, playing an important role in determining the electrochemical performance and the cycling stability, as illustrated in Fig. 1b.

It can be seen that the HTMC-SCS electrode retains over 86.2% of its initial capacitance after repeating galvanostatic charge/discharge tests up to 2000 cycles at a current density of $10\ \text{mA}\ \text{cm}^{-2}$, as shown in Fig. S3, indicating excellent capacitance retention capability. Additionally, we also observed that both the charge transfer resistance and the Warburg impedance related to the ion diffusion process almost remained unchanged while maintaining an excellent capacitive nature (i.e., the phase angle is close to the ideal capacitor phase angle, -90° as shown in the inset of Fig. 3d) after 2000 cycles (Fig. 3d), demonstrating that the HTMC-SCS electrode exhibits excellent electrochemical stability during the charge/discharge process. Moreover, this superior electrochemical stability can be additionally attributed to the architecture that consists of a well-defined core-shell and hollow tubular structure, which can accommodate mechanical stresses that are generated during the charge/discharge process, as indicated in Fig. 3e. In this case, it should be further noted that the presence of an intermixed intermediate region between the CuS core and the NiS shell might significantly contribute towards the maintenance of the structural stability and

integrity of the electrode as well as of the electronic and ionic conductivities. Thus, to understand in detail whether an energetically stable intermediate interlayer can be formed, we first carried out density-functional theory (DFT) calculations (see more detailed information in SI). The structural models for the intermediate interlayer in the HTMC-SCS were constructed based on the $\text{CuS}_{(001)}/\text{NiS}_{(001)}$ planes between their hexagonal crystal structures (Fig. S4). The calculations were performed based upon the assumption that Ni atoms are intermixed within the 1st layer or 2nd layer of the $\text{CuS}_{(001)}/\text{NiS}_{(001)}$ interface, as shown in Fig. 3f. The ratio of Ni atoms on the CuS interface is denoted as interface intermixing from 0.00 to 1.00 monolayer (ML). It is found that the formation energy (ΔE) of all partial ML regions show negative values at both the 1st interlayer and the 2nd interlayer, indicating that Ni atoms can be partially intermixed with CuS to form an energetically stable intermediate state compared to the non-intermixing interface (0.00 ML). In contrast, the ΔE of 1.00 ML (fully covered with Ni atoms) has a positive formation energy, meaning it is an energetically unstable interface. Therefore, it is expected theoretically that the Ni atoms can be energetically intermixed within the CuS layer. In accordance, the high-resolution TEM image of the HTMC-SCS structure clearly shows that the interface between NiS and CuS has an intermediate interlayer region formed from Ni and Cu atoms during the synthesis process (Fig. S5a). Furthermore, we clearly observed that the EDX line profiles of Ni and Cu not only show distinct shell and core regions, but also indicate an intermediate region with a mixed phase of Ni and Cu (Fig. S5b). This confirms the formation of an intermediate interlayer structure in the HTMC-SCS, which can lead to an enhanced adhesion and contact properties at the interface and hence improved structural stability. Additionally, we also carried out SEM analysis after cycling charge/discharge tests so as to estimate the structural stability of the HTMC-SCS. As showed in Fig. S6, the morphology and size of the HTMC-SCS remain without the severe structural collapse

after long-term cycling tests, indicating its excellent structural stability. To further understand core-shell structured hierarchy effects on electrochemically pseudo-capacitive kinetics in the HTMC-SCS electrode, we also prepared the HTMC-SCS with different NiS shell thicknesses under two different concentrations of the Ni precursors, 0.5 and 2.0 M (denoted as HTMC-SCS-L and HTMC-SCS-H, respectively), in comparison to the HTMC-SCS discussed above (denoted as HTMC-SCS-M) fabricated using an 1.0 M Ni precursor. Based on the SEM, STEM, and EDX line-scanning analysis shown in Fig. S7, we confirmed that the NiS is coated along the wall of the CuS nanotubes and that the overall wall thickness of the HTMC-SCS increases (decreases) with increasing (decreasing) concentration of the Ni precursor in comparison with HTMC-SCS-M (Fig. 1e, 2a, and 2b). As expected, it can be clearly seen that all the CV curves of both electrodes with different shell thicknesses show a typical Faradaic redox reaction of $\text{Ni}^{2+}/\text{Ni}^{3+}$ similar to the CV curve for the HTMC-SCS-M electrode (Fig. S8a and S8b). However, the HTMC-SCS electrode exhibits an increase in the charge and discharge time with increasing thickness of the NiS shell in the charge/discharge curves at the same current density, indicating that the volumetric capacitance of the HTMC-SCS-H electrode has the highest value compared to that of other HTMC-SCS electrodes (Fig. 3c, S8c, and S8d).

To further address the role of the shell structure thickness in the pseudo-capacitive kinetics and the electrochemical performance of HTMC-SCS electrodes, we also carried out EIS measurements to investigate the OH^- ion diffusion behavior and electrochemical stability of the HTMC-SCS electrodes with different shell thicknesses. As shown in Fig. 4a, the charge transfer resistance has a tendency to increase with gradually increasing thickness of the NiS shell. In particular, the D of the HTMC-SCS-M electrode, calculated from the Warburg impedance in Fig. S10, is found to be $5.86 \times 10^{-9} \text{ cm}^2 \text{ s}^{-1}$, which is much larger than that of the HTMC-SCS-H electrode (2.14×10^{-9}

cm² s⁻¹). Moreover, as summarized in Fig. 4b, we found that the dynamic electrochemical behavior characteristics of the HTMC-SCS electrodes, such as the rate performance and the cyclability in Fig. S9, are significantly affected by the shell structure as a result of the dependence of the OH⁻ ions diffusivity and the effective charge transfer distance on the shell thickness, as shown in Fig. 4c. Accordingly, designing the shell structure with an adequate thickness is important to maximize the pseudo-capacitive behavior and electrochemical stability by considering the effective diffusion length of the OH⁻ ions into the NiS shell layer, the intrinsic structural stability and capacity of the NiS material, and the effective electron transfer as well as the mechanical stress-mitigating interlayer between the NiS shell and the CuS core. Interestingly, we found that the HTMC-SCS-M electrode exhibits, overall, well-balanced electrochemical properties, such as the relatively improved high-rate retention and a high electrochemical cyclability with a high volumetric capacitance of 18.7 F cm⁻³ after 2000 cycling tests at a current density of 10 mA cm⁻² (Fig. S9b). Combined, this makes it particularly suitable for practical SC applications.

To demonstrate the practical applicability of the well-engineered HTMC-SCS-M electrode for SCs, an asymmetric SC (ASC) was fabricated using active carbon (AC) as an anodic electrode and the HTMC-SCS-M as a cathodic electrode. In order to maximize energy storage performance in the ASC, we systemically designed and evaluated the AC anode electrode by carefully taking into account the overall charge balance between the two electrodes, as shown in Fig. S11. From the CV curves of both the anode and cathode electrodes (Fig. 5a), it is estimated that the AC//HTMC-SCS-M ASC can be operated within a wide operating potential window with a maximum working potential of 1.7 V. Furthermore, when the stable operating potential window is increased from 0.6 to 1.6 V with a step of 0.2 V at a scan rate of 50 mV s⁻¹, the ASC device exhibits a similar

capacitive response without obvious distortion in the CV curves even at the operating potential of 1.6 V (Fig. 5b), showing the excellent charging/discharging capacitive characteristics.

In order to further assess and quantify the electrochemical performance of the AC//HTMC-SCS-M ASC, the galvanostatic charge/discharge measurements were carried out in the selected potential window of 1.6 V at different current densities ranging from 5 to 20 mA cm⁻² (Fig. 5c). The volumetric capacitance of the ASC is estimated to be 7.44 F cm⁻³ at the current density of 5 mA cm⁻², which is much higher than that of other reported ASCs [34-37]. Moreover, the maximum volumetric power and energy densities of the device reach up to 770 mW cm⁻³ and 2.63 mWh cm⁻³, respectively, as highlighted in the Ragone plot (Fig. 5d). Clearly, it can be seen that our ASC device exhibits much higher energy and power densities compared to previously reported Ni-based and Cu-based ACSs and even exceeds the performance of the commercial SC device [38-44]. In addition to energy and power densities, the long-term cycling performance of SCs is another critical factor that needs to be considered for practical applications. Fig. 5e shows the cyclability of our ASC device carried out at a current density of 10 mA cm⁻² over the 10000 cycles. Noticeably, the ASC exhibits superior cycling stability with a capacitance retention of 84.0% even after 10000 cycles, which explicitly demonstrates that our ACS device possesses excellent electrochemical stability. Overall, the remarkably enhanced electrochemical properties of the AC//HTMC-SCS-M ASC are mainly attributed to the well-engineered HTMC-SCS nanoarchitectures with multiple synergistic benefits arising from the unique combination of core-shell material, geometry, and rational design.

3. Conclusions

We have systematically designed and prepared novel hierarchical transition metal chalcogenide architectures with a core-shell and hollow tubular structure for highly capable pseudo-capacitive SCs using a free-standing growth approach. We have demonstrated that the resultant HTMC-SCS heterostructure is composed of a highly conductive and structurally stable CuS core material with a hollow tubular morphology, a highly capacitive NiS shell materials with nanoscale-thick layers on both the inner/outer surface of the CuS core, and energetically stable and good adhesive intermediate layers between the core and the shell. As a result, the optimized HTMC-SCS electrodes displayed a remarkably superior volumetric capacitance of 25.9 F cm^{-3} at a current density of 2 mA cm^{-2} and good rate performance as well as excellent capacitance retention capability. This result might be attributed to the large electrolyte contact areas, the effective diffusion route and distance of the OH^- ions, the high electrical conductivity and low charge transfer resistance, and the mechanical stress-mitigating interlayer and tubular structure, arising from the combined complementary benefits of the unique hierarchical architecture with the combination of core-shell structure and materials. Furthermore, we have also demonstrated that the AC//HTMC-SCS-M ASC exhibits outstanding electrochemical performance with high power (770 mW cm^{-3}) and energy (2.63 mWh cm^{-3}) densities and ultrahigh reversible cyclability (capacitance retention of 84%) over 10000 cycles.

4. Experimental Section

4.1. Fabrication of HTMC-SCS nanoarchitectures.

Copper hydroxide ($\text{Cu}(\text{OH})_2$) nanotubes were synthesized directly on the Cu mesh ($1 \times 1 \text{ cm}^2$ with a thickness of 0.0267 cm, Alfa Aesar) by immersing into the solution with 10.0 M sodium hydroxide (NaOH, 10 mL), 1.0 M ammonium persulfate ($(\text{NH}_4)_2\text{S}_2\text{O}_8$, 5.0 mL) and DI water (22.5

mL). CuS nanotube arrays were then fabricated through the sulfurization of the pre-synthesized $\text{Cu}(\text{OH})_2$ nanotubes with 0.2 M thiourea ($\text{CH}_4\text{N}_2\text{S}$) and subsequent annealing process at 150 °C. After that, HTMC-SCS nanoarchitectures with the NiS/CuS/NiS shell-core-shell nanotubes were obtained by the following sequences: sequentially dipping CuS nanotube samples in (a) nickel(II) chloride hexahydrate ($\text{NiCl}_2 \cdot 6\text{H}_2\text{O}$) solutions and (b) thiourea solutions with different concentrations, 0.5, 1.0, and 2.0 M (denoted as HTMC-SCS-L, HTMC-SCS-M, and HTMC-SCS-H, respectively). The samples were subsequently blow dried with nitrogen gas and then annealed on a hot plate at 150 °C.

4.2. Electrochemical Characterization.

The electrochemical properties of the HTMC-SCS nanostructure directly grown on the Cu mesh were measured in a three-electrode system based on the HTMC-SCS electrodes as a working electrode using a potentiostat (PGSTAT302N, Metrohm, Autolab). For the fabrication of the anode electrodes in the ASC, the slurry was prepared by mixing active carbon as an active material, poly(vinylidene difluoride) as a binder, and Ketjen black as a conductive material, and this was then coated onto the compressed nickel foam as a current collector. All electrochemical analyses of the AC//HTMC-SCS-M ASC were performed using a two electrode system under a 1.0 M KOH solution at room temperature.

ACKNOWLEDGMENT

This research was supported by the Industrial Fundamental Technology Development Program (10052745, Development of the nano-sized (100 nm) manganese ceramic material for high voltage pseudo-capacitor) funded by the Ministry of Trade, Industry and Energy (MOTIE) of Korea, and

the European Research Council under the European Union's Seventh Framework Programme (FP/2007-2013)/Grant Agreement no. 685758, Project '1D-NEON'. In addition, SMM would also like to thank The Royal Society for financial support.

Appendix A. Supporting Information

Additional structural and electrochemical analysis data, and DFT calculation data in Fig. S1-S10 and Table S1-S2.

REFERENCES

- [1] G. Wang, L. Zhang, J. Zhang, *Chem. Soc. Rev.* 41 (2012) 797–828.
- [2] P. Simon, Y. Gogotsi, B. Dunn, *Science* 343 (2014) 1210–1211.
- [3] C. Wu, Y. Xie, *Adv. Mater.* 27 (2015) 3850–3867.
- [4] Z. Yu, L. Tetard, L. Zhai, J. Thomas, *Energy Environ. Sci.* 8 (2015) 702–730.
- [5] J. Shi, X. Li, G. He, L. Zhang, M. Li, *J. Mater. Chem. A* 3 (2015) 20619–20626.
- [6] J. Cai, Z. Li, P. K. Shen, *ACS Appl. Mater. Interfaces* 4 (2012) 4093–4098.
- [7] R. Ramachandran, M. Saranya, P. Kollu, B. P. C. Raghupathy, S. K. Jeong, A. N. Grace, *Electrochim. Acta* 178 (2015) 647–657.
- [8] X. Li, J. Shen, N. Li, M. Ye, *J. Power Sources* 282 (2015) 194–201.
- [9] J. Yang, X. Duan, Q. Qin, W. Zheng, *J. Mater. Chem. A* 1 (2013) 7880–7884.
- [10] X. Yan, X. Tong, L. Ma, Y. Tian, Y. Cai, C. Gong, M. Zhang, L. Liang, *Mater. Lett.* 124 (2014) 133–136.
- [11] J. Yang, X. Duan, W. Guo, D. Li, H. Zhang, W. Zheng, *Nano Energy* 5 (2014) 74–81.
- [12] J. Wu, C. Ouyang, S. Dou, S. Wang, *Nanotechnol.* 26 (2015) 325401.

- [13] D. Ghosh, G. K. Das, *ACS Appl. Mater. Interfaces* 7 (2015) 1122–1131.
- [14] J. Yang, X. Duan, Q. Qin, W. Zheng, *J. Mater. Chem. A* 1 (2013) 7880–7884.
- [15] H. Peng, G. Ma, K. Sun, J. Mu, H. Wang, Z. Lei, *J. Mater. Chem. A* 2 (2014) 3303–3307.
- [16] H. Geng, S. F. Kong, Y. Wang, *J. Mater. Chem. A* 2 (2014) 15152–15158.
- [17] M. H. Kunita, E. M. Girotto, E. Radovanovic, M. C. Goncalves, O. P. Ferreira, E.C. Muniz, A. F. Rubira, *Appl. Surf. Sci.* 202 (2002) 223–231.
- [18] Investing in Mining Stocks, Metals and Commodities. <http://www.infomine.com/investment>, 2016 (accessed 16.09.29).
- [19] Y.-W. Lee, B.-S. Kim, J. Hong, J. Lee, S. Pak, H.-S. Jang, D. Whang, S. N. Cha, J. I. Sohn and J. M. Kim, *J. Mater. Chem. A* 4 (2016) 10084–10090.
- [20] T. Zhu, H. B. Wu, Y. Wang, R. Xu, X. W. Lou, *Adv. Energy Mater.* 2 (2012) 1497–1502.
- [21] Z. Xing, Q. Chu, X. Ren, C. Ge, A. H. Qusti, A. M. Asiri, A. O. Al-Youbi, X. Sun, *J. Power Sources* 245 (2014) 463–467.
- [22] Q. Chu, W. Wang, X. Wang, B. Yang, X. Liu, J. Chen, *J. Power Sources* 276 (2015) 19–25.
- [23] J. F. Moulder, W. F. Stickle, P. E. Sobol, K. D. Bomben, *Handbook of X-ray photoelectron spectroscopy*, Physical Electronics, Inc., Minnesota, 1995.
- [24] L. Chen, J. He, Q. Yuan, Y.-W. Zhang, F. Wang, C.-T. Au, S.-F. Yin, *RSC Adv.* 5 (2015) 33747–33754.
- [25] R. Bhosale, S. Kelkar, G. Parte, R. Fernandes, D. Kothari, S. Ogale, *ACS Appl. Mater. Interfaces* 7 (2015) 20053–20060.
- [26] S.-W. Chou, J.-Y. Lin, *J. Electrochem. Soc.* 160 (2013) D178–D182.
- [27] P. Hao, J. Tian, Y. Sang, C.-C. Tuan, G. Cui, X. Shi, C. P. Wong, B. Tang, H. Liu, *Nanoscale* 8 (2016) 16292–16301.

- [28] H.-J. Ahn, W. B. Kim, T.-Y. Seong, *Electrochem. Commun.* 10 (2008) 1284–1287.
- [29] Y. Jiang, P. Wang, X. Zang, Y. Yang, A. Kozinda, L. Lin, *Nano Lett.* 13 (2013) 3524–3530.
- [30] W. Sun, R. Zheng, X. Chen, *J. Power Sources* 195 (2010) 7120–7125.
- [31] H.-C. Park, K.-H. Lee, Y.-W. Lee, S.-J. Kim, D.-M. Kim, M.-C. Kim, K.-W. Park, *J. Power Sources* 269 (2014) 534–541.
- [32] Y.-W. Lee, D.-M. Kim, S.-J. Kim, M.-C. Kim, H.-S. Choe, K.-H. Lee, J. I. Sohn, S. N. Cha, J. M. Kim, K.-W. Park, *ACS Appl. Mater. Interfaces* 8 (2016) 7022–7029.
- [33] Y.-W. Lee, G.-H. An, B.-S. Kim, J. Hong, S. Pak, E.-H. Lee, Y. Cho, J. Lee, P. Giraud, S. N. Cha, H.-J. Ahn, J. I. Sohn, J. M. Kim, *ACS Appl. Mater. Interfaces* 8 (2016) 17651–17658.
- [34] X. Lu, M. Yu, T. Zhai, G. Wang, S. Xie, T. Liu, C. Liang, Y. Tong, Y. Li, *Nano Lett.* 13 (2013) 2628–2633.
- [35] T. Zhai, F. Wang, M. Yu, S. Xie, C. Liang, C. Li, F. Xiao, R. Tang, Q. Wu, X. Lu, Y. Tong, *Nanoscale* 5 (2013) 6790–6796.
- [36] X. Lu, M. Yu, G. Wang, T. Zhai, S. Xie, Y. Ling, Y. Tong, Y. Li, *Adv. Mater.* 25 (2013) 267–272.
- [37] M. Yu, W. Wang, C. Li, T. Zhai, X. Lu, Y. Tong, *NPG Asia Mater.* 6 (2014) e129.
- [38] D. Yu, K. Goh, H. Wang, L. Wei, W. Jiang, Q. Zhang, L. Dai, Y. Chen, *Nat. Nanotechnol.* 9 (2014) 555–562.
- [39] X. Xiao, T. Li, P. Yang, Y. Gao, H. Jin, W. Ni, W. Zhan, X. Zhang, Y. Cao, J. Zhong, L. Gong, W.-C. Yen, W. Mai, J. Chen, K. Huo, Y.-L. Chueh, Z. L. Wang, J. Zhou, *ACS Nano* 6 (2012) 9200–9206.
- [40] X. Lu, D. Zheng, T. Zhai, Z. Liu, Y. Huang, S. Xie, Y. Tong, *Energy Environ. Sci.* 4 (2011) 2915–2921.

- [41] W. Chen, R. B. Rakhi, H. N. Alshareef, *J. Mater. Chem.* 22 (2012) 14394–14402.
- [42] Z.-S. Wu, W. Ren, D.-W. Wang, F. Li, B. Liu, H.-M. Cheng, *ACS Nano* 4 (2010) 5835–5842.
- [43] W. Zilong, Z. Zhu, J. Qiu, S. Yang, *J. Mater. Chem. C* 2 (2014) 1331–1336.
- [44] P. Yang, X. Xiao, Y. Li, Y. Ding, P. Qiang, X. Tan, W. Mai, Z. Lin, W. Wu, T. Li, H. Jin, P. Liu, J. Zhou, C.P. Wong, Z.L. Wang, *ACS Nano* 7 (2013) 2617–2626.

Figure Captions

Fig. 1. (a) Radar plots to present the important factors of NiS and CuS for evaluating the combination of core-shell materials in pseudo-capacitive SCs. (b) Illustration of the proposed hierarchical transition metal (Cu and Ni) chalcogenide core-shell electrode highlights the electrochemical behavior and performance of the different components. SEM images of (c) Cu(OH)₂ nanotubes, (d) CuS nanotubes, and (e) HTMC-SCS nanoarchitectures prepared using a hierarchical bottom-up synthetic processes. The inset in Fig. 1c clearly shows that the tip of the Cu(OH)₂ nanotubes is hollow. XRD patterns of the (f) Cu(OH)₂ nanotubes, (g) CuS nanotubes, and (h) HTMC-SCS nanoarchitectures.

Fig. 2. (a) TEM images, (b) EDX line-scanning profiles, and (c) scanning TEM (STEM) and EDX mapping images for the Cu (red), Ni (blue), and S (green) in the HTMC-SCS nanostructure. **The all scale bars in Figure 2a and 2c are 50 nm.** XPS (d) Cu, (e) Ni, and (f) S spectra of the HTMC-SCS nanostructure.

Fig. 3. (a) CV curves for the HTMC-SCS electrode at 10 mV s⁻¹ in a 1.0 M KOH electrolyte. The inset indicates the CV curve of the CuS electrode. (b) CV curves for the HTMC-SCS electrode at different scan rates from 5 to 50 mV s⁻¹. (c) Galvanostatic charge/discharge curves for the HTMC-SCS electrode at different current densities from 2 to 20 mA cm⁻². (d) Nyquist plots of the HTMC-SCS electrode before and after cycling tests. The inset indicates the Bode plot for the phase before and after cycling. (e) Illustration highlighting the structural benefits that enable the enhanced electrochemical stability in the HTMC-SCS electrode. (f) Calculated formation energy (ΔE) for

interface intermixing at the $\text{CuS}_{(001)}/\text{NiS}_{(001)}$ planes using DFT calculations. Images of the optimized intermixed structure on the 1st interlayer (left) and 2nd interlayer (right).

Fig. 4. (a) Nyquist plots for all three HTMC-SCS electrodes with different shell thicknesses. (b) A comparison of the various electrochemical characteristics such as diffusion coefficient, capacitance and rate retentions, and volumetric capacitance for all three HTMC-SCS electrodes. These electrochemical parameters are obtained from the results shown in Fig. S8 and S9. (c) Illustration of the dynamic pseudo-capacitive characteristics of the HTMC-SCS electrodes with different shell thicknesses.

Fig. 5. (a) Comparative CV curves of AC and HTMC-SCS-M at 50 mV s^{-1} . (b) CV curves of the AC//HTMC-SCS-M ASC in different upper potentials from 0.6 to 1.6 V at a scan rate of 50 mV s^{-1} . (c) Galvanostatic charge/discharge curves of the ASC under various different current densities. (d) Ragone plots related to energy and power densities of the AC//HTMC-SCS-M ASC for a comparison with other recently reported pseudo-capacitive SCs. (e) Cycling performance of the ASC at a current density of 10 mA cm^{-2} up to 10000 cycling charge/discharge tests.

Fig. 1. Y.-W. Lee et al.

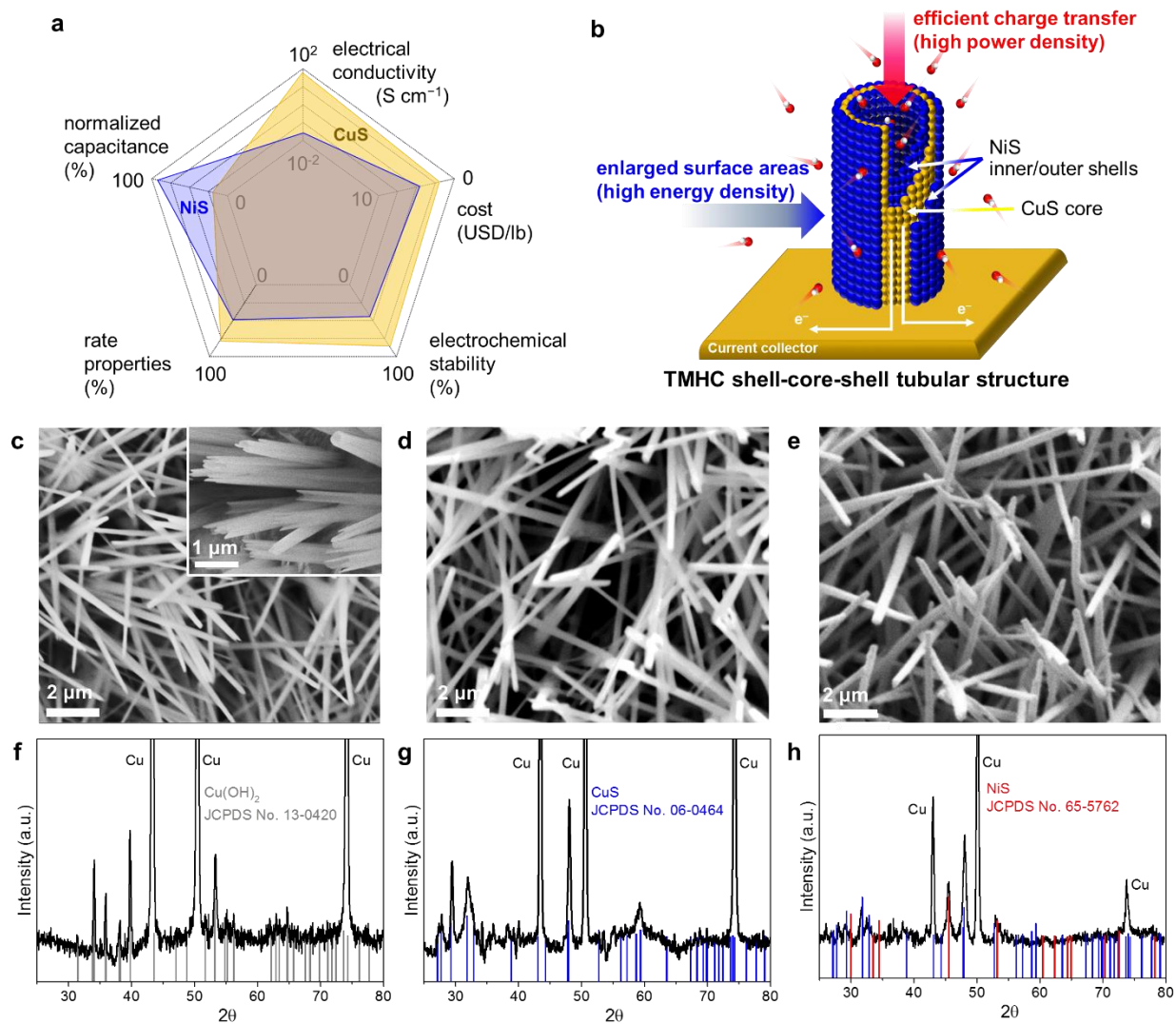


Fig. 2. Y.-W. Lee et al.

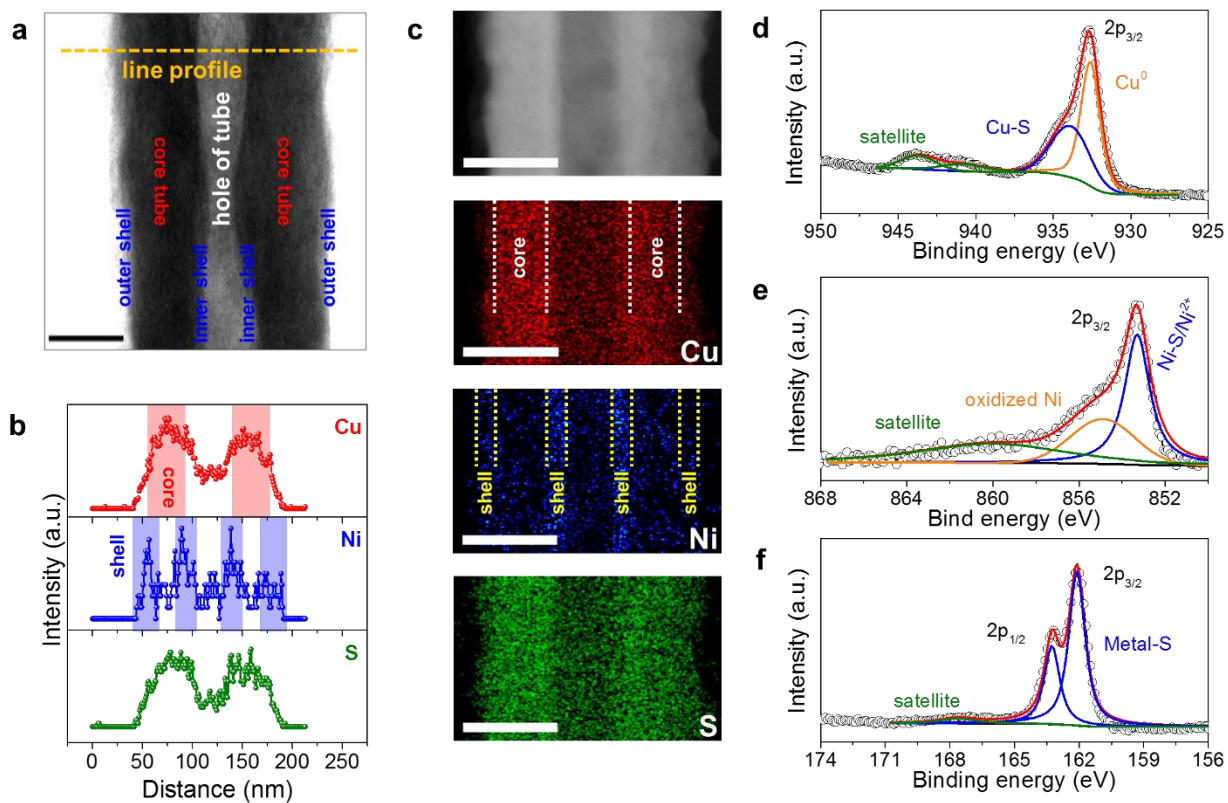


Fig. 3. Y.-W. Lee et al.

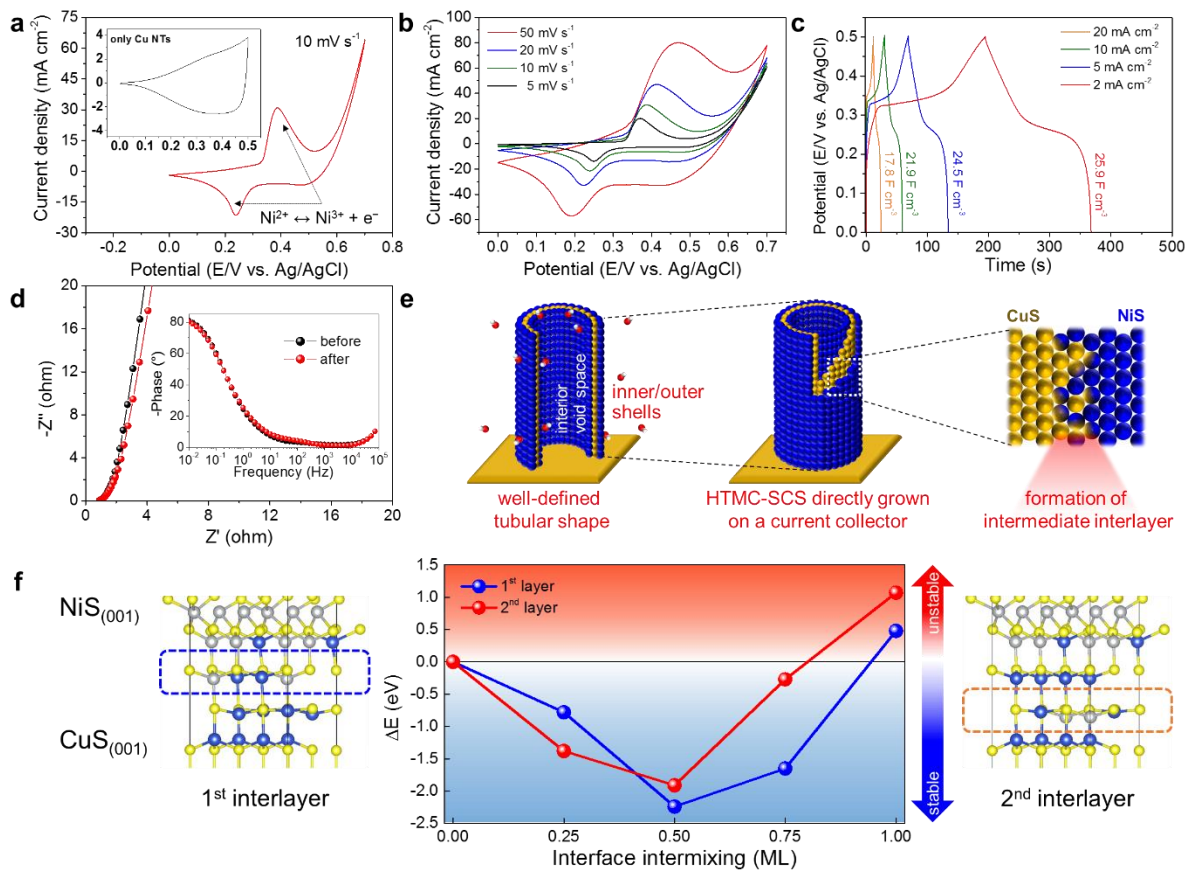


Fig. 4. Y.-W. Lee et al.

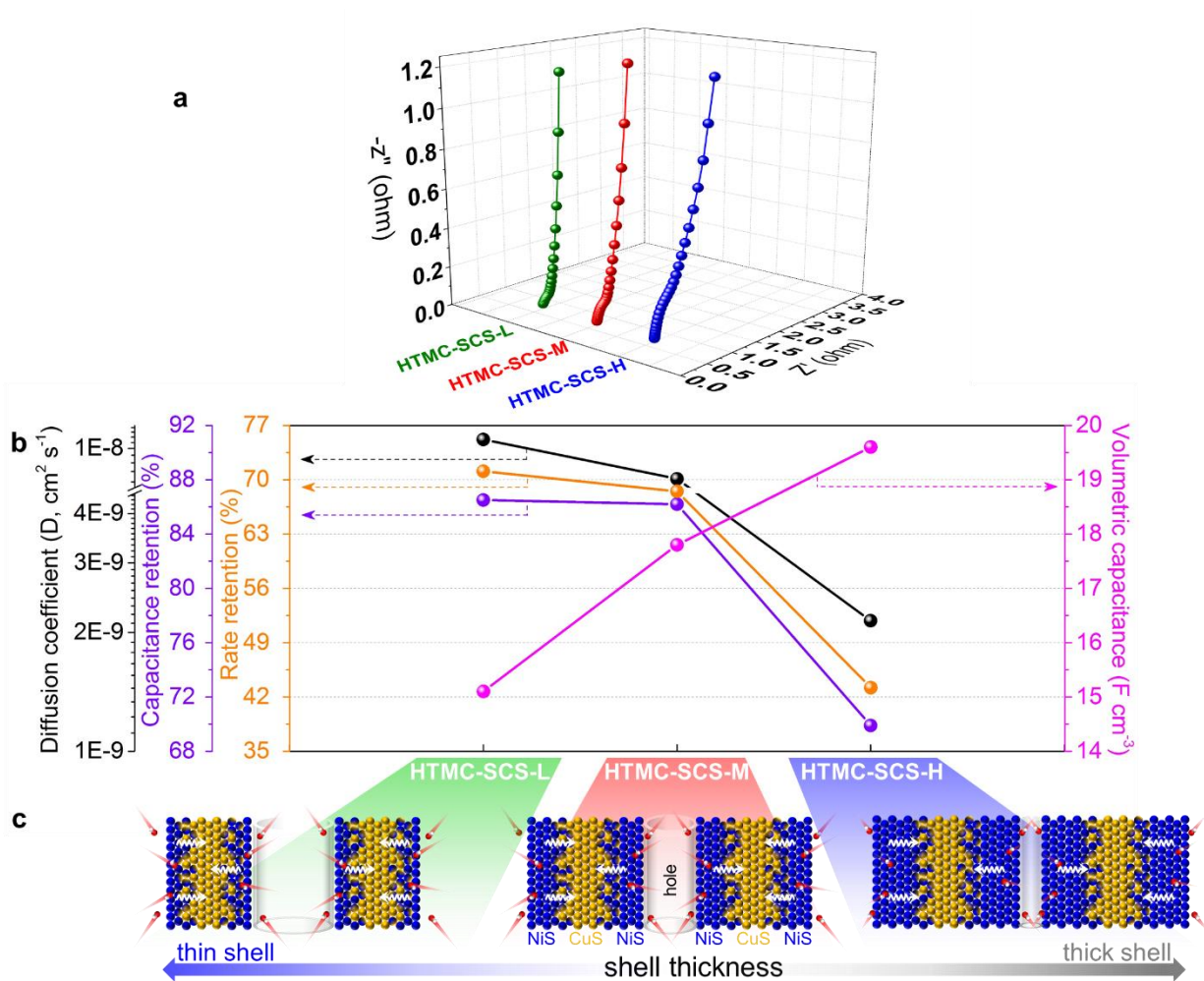


Fig. 5. Y.-W. Lee et al.

